ACS OMEGA

http://pubs.acs.org/journal/acsodf

Article

Starch-Assisted Synthesis of Bi_2S_3 Nanoparticles for Enhanced Dielectric and Antibacterial Applications

Imran Uddin,[#] Shaik M. Abzal,[#] Kurapati Kalyan, Sailakshmi Janga, Ashutosh Rath, Rajkumar Patel, Deepak K. Gupta, T. R. Ravindran, Hira Ateeq, Mohd Sajid Khan, and Jatis K. Dash*

Cite This: *ACS Omega* 2022, 7, 42438−42445

Read Online

ACCESS | Metrics & More | Article Recommendations

ABSTRACT: Starch $[(C_6H_{10}O_5)_n]$-stabilized bismuth sulfide (Bi_2S_3) nanoparticles (NPs) were synthesized in a single-pot reaction using bismuth nitrate pentahydrate ($Bi(NO_3)_3{\cdot}5H_2O$) and sodium sulfide (Na_2S) as precursors. Bi_2S_3 NPs were stable over time and a wide band gap of 2.86 eV was observed. The capping of starch on the Bi_2S_3 NPs prevents them from agglomeration and provides regular uniform shapes. The synthesized Bi_2S_3 NPs were quasispherical, and the measured average particle size was ∼11 nm. The NPs are crystalline with an orthorhombic structure as determined by powder X-ray diffraction and transmission electron microscopy. The existence and interaction of starch on the NP's surface were analyzed using circular dichroism. Impedance spectroscopy was used to measure the electronic behavior of Bi_2S_3 NPs at various temperatures and frequencies. The dielectric measurements on the NPs show high dielectric polarizations. Furthermore, it was observed that the synthesized Bi_2S_3 NPs inhibited bacterial strains (*Bacillus subtilis*, *Escherichia coli*, *Pseudomonas aeruginosa*, and *Staphylococcus aureus*) and demonstrated substantial antibacterial activity.

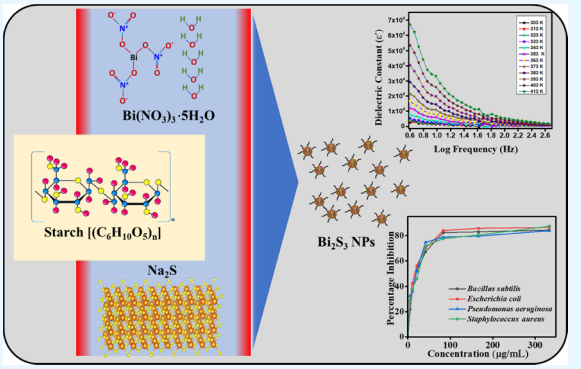

1. INTRODUCTION

Bi_2S_3 is a two-dimensional layered material from the stibnite family that has the potential to be used in electrical smart device applications in the future. Bismuth sulfide (Bi_2S_3) is one of the prominent V−VI semiconductors, having a direct band gap of 1.3 eV among the several metallic sulfides. It is a layered material with a lamellar structure made up of alternating infinite chains of Bi^{3+} and S^{2-}, and it crystallizes out, preferring the orthorhombic system.[1] Because of its numerous essential applications, such as photovoltaic materials, photodiode arrays, thermoelectric devices, and nonlinear optical devices and sensors, Bi_2S_3 has received a lot of attention.[2−4] In addition, it has good electrochemical hydrogen storage capabilities and is employed in biomedical sciences as an imaging agent in X-ray computed tomography.[5]

Metal sulfides are distinguished among nanomaterials because of their exotic optical, electrical, and magnetic characteristics. These physical and chemical features are dependent on their shape, size, crystal phases, and most importantly the synthesis routes. Bi_2S_3 nanoparticles have been made using a variety of techniques, including ultrasonic method,[6] microwave-assisted route,[7] photochemical synthesis method,[8] thermal decomposition,[9] and solvothermal/hydrothermal processes.[10]

The nonaqueous techniques for Bi_2S_3 NP synthesis have many disadvantages as they require complex instruments, costly solvents and templates, powerful surfactants, and high reaction temperatures. Furthermore, since biomedical research is conducted in water as a solvent, the nonaqueous Bi_2S_3 NPs have practical limits in a variety of applications, particularly in the field of biomedicine. In order to synthesize water-dispersible NPs that are biocompatible, extremely stable, and less toxic and have good optical properties, it is crucially important that a green process be used. Biomolecule-assisted synthesis of Bi_2S_3 NPs is a promising method to address the above challenges. A biomolecule-assisted production of single-crystalline Bi_2S_3 nanostructures was reported by Zhang et al.[11] In this study, the amino acid cysteine is used as a sulfur precursor and a capping agent in the growth of Bi_2S_3 nanocrystals. In another study, under microwave irradiation, Lu et al. employed a long polypeptide to synthesize the well-organized snowflake shape of Bi_2S_3 nanorods.[12] The

Received: August 30, 2022
Accepted: October 26, 2022
Published: November 8, 2022

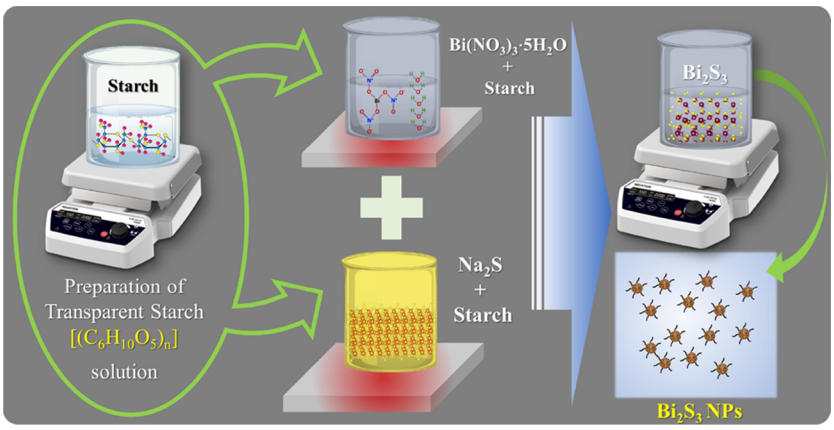

Figure 1. Schematic depiction of the starch-assisted synthesis of Bi_2S_3 NPs.

glutathione molecule was employed as a sulfur source as well as an assembly molecule. Under stress conditions, biomolecules secreted by the fungus *Fusarium oxysporum* were used by Uddin et al. to make Bi_2S_3 nanoparticles (NPs). These Bi_2S_3 NPs were also employed in small-animal single-photon emission computed tomography probes.[13] The synthesis of biomolecule-capped metal sulfides (such as CdS QDs, ZnS QDs, and CuS NPs) was reported previously.[14−16]

Semiconductor NPs having biological cappings are gaining popularity as effective antibacterial agents with a broad variety of applications and biocompatibility, making them excellent candidates for pharmaceutical and biomedical use. Furthermore, starch renders the NPs biocompatible and extremely permeable to live cells. A built-in electric field was recently identified for an interfacial Schottky junction of $Bi_2S_3/Ti_3C_2T_x$. Under 10 min of 808 nm NIR light irradiation, it had 99.86% (against *Staphylococcus aureus* (*S. aureus*)) and 99.92% (against *Escherichia coli* (*E. coli*)) photoresponsive bacteria-killing efficacies. Bacterial strains were suppressed by the synthesized Bi_2S_3 NPs, demonstrating their significant antibacterial activity.[17]

In the present study, we have synthesized Bi_2S_3 NPs by adopting an easy and efficient method by utilizing starch $[(C_6H_{10}O_5)_n]$, which serves as a capping and reducing agent. Inside an aqueous medium, starch acts as a stabilizer, preventing agglomeration and imparting stability and monodispersity to Bi_2S_3 NPs. It attaches to the surface of as-synthesized NPs, limiting particle nucleation and growth to certain sizes. It was also observed that the NP solution was exceptionally stable, with little aggregation even after a month. Furthermore, impedance spectroscopy was employed to investigate the conductivity and dielectric constants of Bi_2S_3 NPs at various temperatures, frequencies, and applied fields. We also explored the antibacterial properties of Bi_2S_3 NPs and measured the minimum inhibitory concentrations (MICs) against the bacterial strains.

2. EXPERIMENTAL SECTION

Starch soluble (CAS No: 9005-84-9) of AR grade was purchased from SRL Ltd. and used as received without any further purification. Merck Ltd. provided bismuth(III) nitrate pentahydrate $Bi(NO_3)_3{\cdot}5H_2O$ and SRL Ltd. provided sodium sulfide (Na_2S). The aqueous solutions were prepared with Milli-Q water for all the experiments.

2.1. Synthesis of Bi_2S_3 NPs. Bismuth nitrate pentahydrate ($Bi(NO_3)_3{\cdot}5H_2O$), starch soluble, and Na_2S flakes (with more than 99% purity) were used in the synthesis of Bi_2S_3. For all the experiments, Milli-Q water was used to make the aqueous solutions. In a typical procedure, 0.5 g of starch was mixed with 100 mL of Milli-Q water and heated to 70−80 °C with stirring for 20 min, yielding a clear starch solution. The transparent starch solution was divided into two parts equally. Then, 0.05 M $Bi(NO_3)_3{\cdot}5H_2O$ was dissolved in 50 mL of starch solution followed by heating at 70 °C for 20 min while stirring. Similarly, Na_2S (0.0976 g, 0.05 M) was dissolved in 50 mL of a hot starch solution separately. Furthermore, a dark brownish-black color appeared in the reaction mixture after the addition of a hot Na_2S solution (in drops) to bismuth nitrate solution while stirring it at 90 °C for 20 min, indicating the formation of Bi_2S_3. The Bi_2S_3 NPs were washed with Milli-Q water before being used for further measurements. As seen in Figure 1, the facile synthesis of Bi_2S_3 NPs with the use of starch as a stabilizing agent is depicted in a vivid scheme.

2.2. Experimental Characterizations. A Multiskan GO spectrophotometer (Thermo Scientific, USA) was used to record the UV−visible absorption spectra over a wavelength range of 200−900 nm with a resolution of ∼1 nm. To characterize the crystal structure and average grain size, powder X-ray diffraction (XRD) ($\theta - 2\theta$) scans were recorded for the drop-cast sample on a glass substrate using a PANalytical Empyrean series X-ray diffractometer equipped with a Bragg−Brentano setup, a fast solid-state (PIXcel3D) X-ray detector. The X-ray beam from Cu Kα radiation (with λ = 1.5406 Å) was used to scan in the 2θ range of 20−70° with a step size of 0.02° and a time per step of 20 s. Furthermore, the vibrational modes were examined by Raman spectroscopy. Raman spectra were obtained using an excitation wavelength of 514.5 nm line of an Ar^+ laser using a micro-Raman spectrometer (Renishaw, UK, model inVia) in the back-scattering geometry. The dynamic light scattering (DLS) and zeta potential measurements were carried out using a Zetasizer (Nano series) instrument. The measured scattering light intensity is displayed as a photon count rate with a unit of kilo counts per second (kcps). All average particle sizes reported here are based on the scattered light intensity weighted averages.

Bi_2S_3 NPs suspended in an aqueous solution were transferred to carbon-coated copper grids. A transmission electron microscopy (TEM) investigation was carried out using a JEOL JEM 200F TEM operated at 200 kV. The far-UV circular dichroism (CD) experiment was carried out using a Jasco CD J-1500 instrument. CD spectra were recorded using

https://doi.org/10.1021/acsomega.2c05593
ACS Omega 2022, 7, 42438−42445

Spectra Manager software for a wavelength range of 190−250 nm. Each spectrum was taken by averaging three scans, and all the scans were collected at an interval of 1 nm wavelength. CD spectra were recorded with a scan speed of 20 nm/min and a response time of 1 s. Fourier transform infrared (FTIR) measurements were performed using a Jasco FT/IR-4700 over a scanning range of 400−4000 cm^{-1} at a resolution of 4.0. Impedance measurements were performed using a Hioko IM3536 impedance analyzer with a 1 Hz−8 MHz frequency range and a temperature range of 300−473 K. The impedance spectroscopy was performed on a sintered pellet of Bi_2S_3 NPs that has been pressed into a pellet using a hydraulic press under a load of 3 tons for 2 min. The temperature of the pellet was made stable for 4 to 5 min before taking each measurement.

The antibacterial activities of Bi_2S_3 NPs were evaluated using the well diffusion method. Also, their potency was analyzed by calculating the MIC and minimum bactericidal concentration using the microdilution method. National Collection of Industrial Microorganisms, Pune, India provided *S. aureus* (ATCC 25923), *E. coli* (ATCC 25922), and *Pseudomonas aeruginosa* (*P. aeruginosa*, ATCC 27853). The bacterial cultures were grown to the mid-logarithmic phase and harvested after centrifuging at 6000 *g* for 10 min. Then they were washed with 20 mM sodium phosphate buffer at a pH value of 7.4. Approximately 2×10^5 colony forming units (CFU)/mL of the abovementioned bacterial strains were inoculated on Luria−Bertani (LB) agar plates. Wells were made using a sterile cork borer (3 mm in radius) in agar plates having inoculums. Then, 100 μL of Bi_2S_3 NP solution and Milli-Q water as a control were added to the respective wells on the seeded agar plate. The widths of the inhibitory zones were analyzed, and optical micrographs of the plates were taken after incubating for 24 h at 37 °C. The Bi_2S_3 NPs were diluted in 50 μL of LB medium in 96-well microtiter plates to obtain the concentrations (0−50 g/mL) with the bacterial inoculum to determine the MIC (5×10^4 CFU per well). The MIC was calculated as the lowest concentration of nanomaterials with which growth inhibition occurred during an overnight incubation at 37 °C.

The cell culture study was carried out on a normal rat kidney epithelial (NRK) cell line procured from National Centre for Cell Science, Pune, India. The DMEM-F12 medium was selected for NRK cells and was enriched with 12% sterilized FBS and 1.5% antibiotic−antimycotic solutions containing penicillin, streptomycin, and amphotericin B (Himedia India Ltd., Mumbai, India). The cells were incubated in a humidified chamber with 5% CO_2 at 37 °C.

The cytotoxicity of Bi_2Si_3 NPs was evaluated against the NRK cell line using the MTT assay. The HK-2 cells were seeded at a density of 5×10^3 cells/well in 96-well plates at 37 °C for 24 h in a humidified chamber with 5% CO_2. Eventually, these adherent cells were treated with Bi_2Si_3 NPs at different concentrations and incubated for 24 h. Subsequently, the treated cells were incubated with 10 μL of 5 mg/mL MTT dye for 2 h at 37 °C. Then, formazan crystal (purple colored) precipitates were obtained, which were subsequently dissolved in 90 μL of dimethyl sulfoxide. The absorbance of the dissolved crystals of each well was measured at 570 nm. The cell inhibition percentage was evaluated over the untreated cell. The IC_{50} value was evaluated by calibrating the graph between concentration and absorbance on Origin 6.0 Professional.

3. RESULTS AND DISCUSSION

3.1. Optical Properties of Bi_2S_3 NPs. UV−vis absorption and photoluminescence spectra were analyzed to investigate the optical properties of Bi_2S_3 NPs. Curve 1 in Figure 2a exhibits a strong absorption shoulder centered at 310 nm, which corresponds to the excitonic transition in Bi_2S_3 nanocrystallites.[18] Because of the production of particles of various sizes, there is no absorption edge. The quantum size confinement in Bi_2S_3 NPs and the widening of the energy gap between the valence and conduction bands are additional factors to it. By fluorescence measurement of Bi_2S_3 NPs excited at 310 nm, the luminescence properties of Bi_2S_3 NPs were investigated. In contrast to the emission peaks of Bi_2S_3 NPs, an emission band centered at 365 nm was found in curve 2 in Figure 2a, which may be ascribed to the band gap or near band gap emission caused by the recombination of electron−hole pairs in the Bi_2S_3 NPs.[19] The emission spectrum in Figure 2a curve 2 indicates wide emission that does not cease at zero intensity as the wavelengths increase. The immobilization of charge carriers causes this emission phenomenon, which leads to surface energy traps. Bi_2S_3 is known to be a direct band gap semiconductor. The band gap of Bi_2S_3 NPs was estimated using the absorption coefficient as a function of wavelength using the "Tauc equation". The $(ah\nu)^2$ versus $(h\nu)$ graph is shown in Figure 2b, and a tangent was drawn on the energy axis by extrapolating the linear component. The Tauc plot produced from the Bi_2S_3 UV−visible spectrum reveals that the band gap value is roughly 2.86 eV, which is much greater than the band gap energy of bulk Bi_2S_3, which is 1.3 eV.[20] The decrease in the size of Bi_2S_3 NPs causes an increase in the band gap energy, which may be a prominent consequence of the size quantization effect. When a particle's size shrinks, discretization of subbands occurs in the valence and conduction bands; as a result, the energy levels become quantized. Because of the larger surface area of the NPs at their lower size, the emission occurs from holes and electrons trap near the surface of the NPs. This might cause a blue shift in the energy of the photoluminescence spectrum.

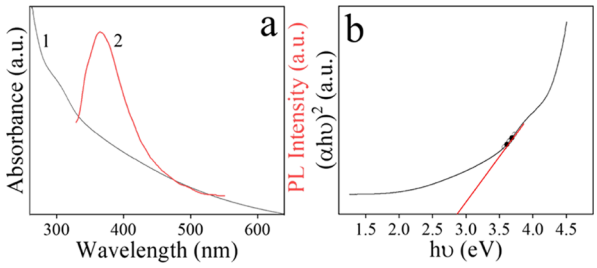

Figure 2. (a) UV−visible spectrum of Bi_2S_3 NPs (curve 1) and photoluminescence emission spectrum of Bi_2S_3 NPs (curve 2). (b) Tauc plot of Bi_2S_3 NPs obtained after the analysis of the UV−visible spectrum of Bi_2S_3 NPs. Bi_2S_3 NPs' band gap energy is represented by the tangent drawn on the absorption edge.

3.2. Structural Properties. The XRD scans were acquired from the drop-coated films of Bi_2S_3 NPs on a glass substrate to investigate the crystallinity of Bi_2S_3 NPs. In Figure 3a, the top image shows the side view of the Bi_2S_3 crystal, which shows the layered nature in the *c* direction. The bottom image shows the top view of the orthorhombic structure. The XRD patterns were analyzed and indexed (shown in Figure 3b, curve 1). The peak positions (2θ values) coincide with those reported for

https://doi.org/10.1021/acsomega.2c05593
ACS Omega 2022, 7, 42438−42445

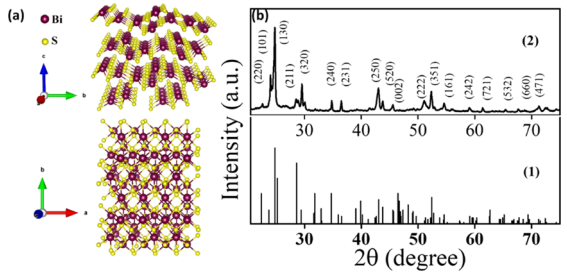

Figure 3. (a) Side view and Top view of Bi_2S_3 crystal (b) Powder XRD patterns of the Bi_2S_3 NP powder. The powder Bragg reflections were identified, and indexing was done with the corresponding crystal planes.

Bi_2S_3 NPs.[21] All the peaks in the pattern are identified to the orthorhombic phase of Bi_2S_3 (JCPDS No: 170-320) with the space group *pnma* having the lattice parameters *a*, *b*, and *c* as 4.02, 11.17, and 11.73 Å, respectively (shown in Figure 3b curve 2). The peak widening in the XRD spectra is seen in the patterns, indicating that the crystallites are tiny. The Debye–Scherrer formula $\left(D = \frac{k\lambda}{\beta \mathrm{Cos}\theta}\right)$ was used to calculate the mean crystallite size of Bi_2S_3 NPs, where D is the grain size, λ is the wavelength, k is a shape factor with a value of 0.9, β is the full width at half maximum (FWHM) of the corresponding XRD peak, and θ is the Bragg angle. The mean particle size of Bi_2S_3 NPs was measured as ∼12 nm. A comprehensive electron microscopy analysis was conducted on the as-synthesized Bi_2S_3 NPs to further investigate their structural morphology. It was observed that the formed Bi_2S_3 NPs are quasi-spherical in shape (Figure 4a). The average particle size was calculated to be around 11 nm, according to the DLS graph (Figure 4b). Because the Bi_2S_3 NPs are stabilized by the starch present on the surface, these NPs appear to be well separated from one another. Here, starch acts as a capping layer on the surface and prevents the agglomeration of NPs to form bigger clusters.

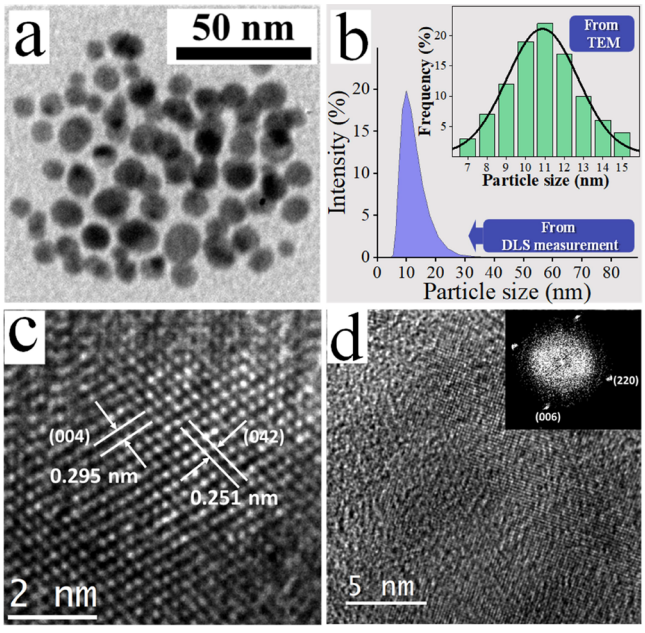

Figure 4. (a) TEM image, (b) DLS data and particle size distribution (inset), (c) HRTEM lattice interplanar spacing, and (d) fast Fourier transform (FFT) of the Bi_2S_3 NP real space image.

The particle size histogram of Bi_2S_3 NPs (inset of Figure 4b) showed that the NPs are in the range of 7−15 nm, with an average size of ∼11 nm. High-resolution transmission electron microscopy (HRTEM) real space images were obtained to examine the crystallinity at the single QD level. The HRTEM image of the as-synthesized Bi_2S_3 NPs is presented in Figure 4c. The interplanar spacings correspond to the (004) and (042) planes of the Bi_2S_3 orthorhombic crystal structure. All the Bi_2S_3 NPs were found to be incredibly crystalline.

The FFT pattern of the real space image further validated the crystallinity of the as-synthesized Bi_2S_3 NPs (Figure 4d). We analyzed and indexed the FFT spots as (220) and (006) for the orthorhombic phase, where the value of the *d*-spacing obtained well matched with the reported values.[22] The energy-dispersive X-ray (EDX) analysis reveals that the Bi_2S_3 NPs have Bi and S in the proportions of 29.78 and 49.77% atomic percentage, respectively.

Figure 5 shows the Raman shift spectra obtained from the Bi_2S_3 NPs. A multi-Lorentzian fitting was carried out for the

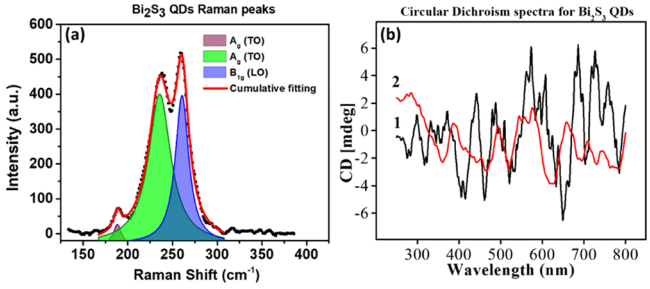

Figure 5. (a) Raman spectra obtained from the Bi_2S_3 NP drop-coated films. The red curve is the multi-Lorentzian fitting, and the other shaded curves correspond to the vibrational modes A_g and B_{1g} as shown. (b) CD spectra of starch soluble (curve 1) and starch-functionalized Bi_2S_3 NPs (curve 2).

identification and determination of the Raman band positions. The obtained peak positions correspond to the A_g (at 186 and 236 cm^{-1}) and B_{1g} (at 259 cm^{-1}) optical modes. The analyzed A_g and B_{1g} modes are associated with the transverse optical (TO) and longitudinal optical (LO) phonons, respectively, agreeing well with the earlier reported Raman signals specifically from Bi_2S_3 NPs.[23] The Raman peak positions and FWHM analyzed from the peaks are listed in Table 1.

Table 1. Raman Peak Positions and FWHM for the Observed Vibrational Modes

vibrational modes	Raman shift (cm^{-1})	FWHM (cm^{-1})
A_g (TO)	186	11
A_g (TO)	236	30
B_{1g} (LO)	259	18

Starch is a polysaccharide made up of one and four linkages between glucose monomers. As mentioned earlier, the chemical formula of the starch molecule is $(C_6H_{10}O_5)_n$. Amylose was the first biopolymer known to exist as a helix in the solid state. An optical rotatory dispersion method (CD) was used to determine the change in the helical conformation of starch. As shown in Figure 5b, the characteristic peaks of starch independent of carbon lengths are 372 and 489 nm. The other peaks which vary with the change in carbon lengths are 443, 574, 607, 686, 727, and 760 nm.[24] The interaction of

https://doi.org/10.1021/acsomega.2c05593
ACS Omega 2022, 7, 42438−42445

Bi_2S_3 NPs with starch can be inferred by the shifting of peaks of pure starch from 298, 371, 488, and 726 to 386 nm, 387, 496, and 743 nm, respectively, by exciton interactions. The complex of starch−Bi_2S_3 NPs can be characterized by peaks at 360, 464, and 576 nm with a shoulder at 477 nm other than the maxima.[25] The main bands of the complex (starch−Bi_2S_3 NPs) at 372 nm and at 489 nm are assigned to $\pi \rightarrow \sigma^*$ and $\pi^* \rightarrow \sigma^*$ transitions, respectively.

The formation of Bi_2S_3 NPs and their functionalization by starch molecules were investigated by FTIR spectroscopy, as shown in Figure 6. The broad absorption band in the 500−700

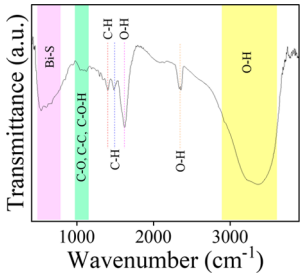

Figure 6. FTIR spectrum of Bi_2S_3 NPs.

cm^{-1} range, which is the representative region of metal sulfide bonds, was assigned to the Bi−S vibration. We employed the starch solution as a stabilizing (and capping) agent in the synthesis of Bi_2S_3 NPs. The FTIR spectrum showed that the strong broad absorption peak regions between 3300−3400 and 1637 cm^{-1}, respectively, were attributed to the −OH stretching and bending vibration modes caused by the formation of hydrogen bonds of the water molecules on the surface of the sample. The other characteristic bands were observed at wavenumbers of 1460 and 1383 cm^{-1} due to C−H symmetric bending. The bonds connected to C−O stretching at 900−1200 cm^{-1} in starch-capped Bi_2S_3 NPs displayed a wider absorption band range, and it is always feasible that chemical interactions may also take place in this bonding area. These absorption bands are associated with starch's C−O, C−C, and C−O−H bending vibrations. The bond C−O−C, in particular, was assigned to the asymmetrical stretching of the glycosidic linkage and stretching vibration of the glucose ring, whereas the bond C−O−H was assigned to carboxylic stretching.

Zeta potential measurements for the starch-stabilized Bi_2S_3 NPs were also carried out. The OH group of the capping agent is revealed to be the cause of the negative zeta potential value of the starch-stabilized Bi_2S_3 NPs. Bi_2S_3 NPs' zeta potential was found to be −15.7 mV (Figure 7). This gives stability to the

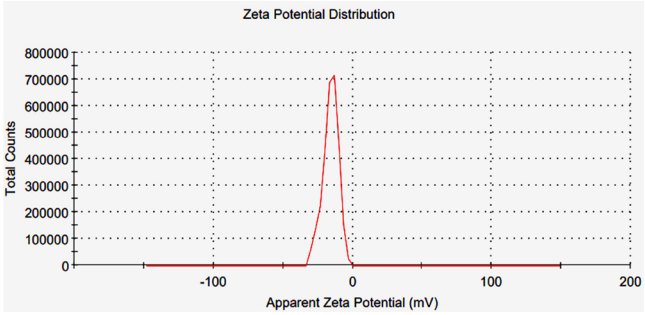

Figure 7. Zeta potential of starch-capped Bi_2S_3 NPs.

NPs in an aqueous solution over a long term. Also, clump and agglomeration development may be avoided by keeping NPs away from the repelling electrostatic forces.

3.3. Antibacterial Study. Zones of inhibition experiments against *Bacillus subtilis* (*B. subtilis*), *E. coli*, *P. aeruginosa*, and *S. aureus* were performed on LB plates to assess the antibacterial activity of Bi_2S_3 NPs. As illustrated in Figure 8, Bi_2S_3 NPs

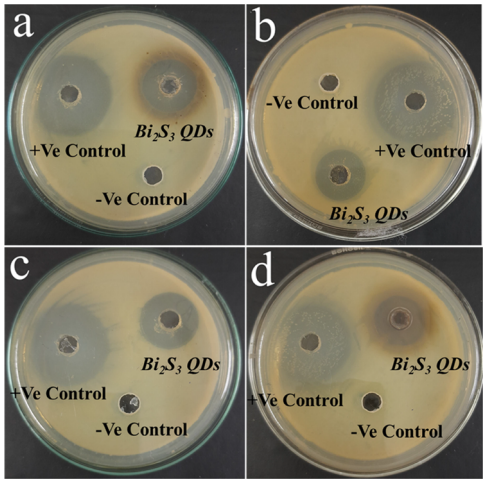

Figure 8. LB agar plates showing zone of inhibition of bacterial colonies: (a) *B. subtilis*, (b) *E. coli*, (c) *P. aeruginosa*, and (d) *S. aureus*.

showed good clearing zones surrounding the wells and required fewer dosages for a variety of antibacterial applications. In the wells containing Milli-Q water, used as a negative control, there was no zone of clearing in the control response. However, the wells that had antibiotics in them, which were used as a positive control, seemed to have a large area of cleanup.[26]

With MICs of 19.42, 16.75, 18.73, and 23.45 μg/mL, the Bi_2S_3 NPs were shown to be very efficient against *B. subtilis*, *E. coli*, *P. aeruginosa*, and *S. aureus*, respectively (see Figure 9).

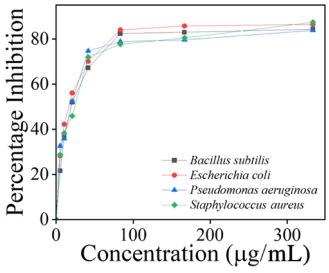

Figure 9. MICs of Bi_2S_3 NPs against (a) *B. subtilis*, (b) *E. coli*, (c) *P. aeruginosa*, and (d) *S. aureus* bacterial strains.

The findings clearly show that Bi_2S_3 was more active against G + than G−. The cell wall of G− bacteria is composed of phospholipids, lipoproteins, and LPS, which function as a penetrating barrier. In contrast, the presence of a thin coating of peptidoglycan and teichoic acid as well as many holes renders the cell wall of G+ bacteria vulnerable to the entrance of foreign materials. To do this, it has been shown that Bi_2S_3 NPs are more active against G+ bacteria and can generate holes in the cell wall.

Furthermore, it is known that nanomaterials, in general, create an excessive amount of reactive oxygen species (ROS),

https://doi.org/10.1021/acsomega.2c05593
ACS Omega 2022, 7, 42438−42445

which are responsible for nonspecific DNA, lipid, and protein damages in the cell. The interaction of nanomaterials with the cell walls of bacteria results in the production of a wide range of ROS.[27]

The antibacterial activity of nanomaterials is also connected with the size of the nanomaterials, the presence of charged groups, the presence of sharp edges, and the presence of the orthorhombic phase. Thus, the attachment of bacterial cells to the Bi_2S_3 NPs results in the production of ROS, which ultimately leads to the destruction of bacterial cells.

The cytotoxicity evaluation of Bi_2S_3 NPs against the NRK cell line was found to be satisfactory (Figure 10). The cells

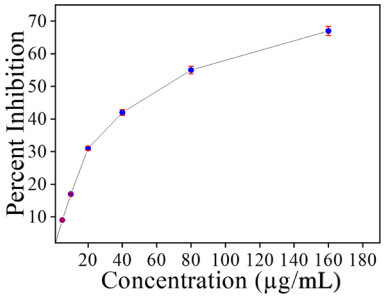

Figure 10. Graphs showing cytotoxicity (dose dependent) of Bi_2S_3 NPs against NRK cells.

were found to show IC_{50} values at a 64.8 μg/mL concentration, whereas the bacterial inhibitions were achieved at much lower concentrations. Eventually, with an increase in the concentration, inhibition was found to increase very slowly and was only 67% at a 180 μg/mL concentration.

3.4. Impedance Spectroscopy Measurements. The Nyquist plots (imaginary vs real part of impedance) of Bi_2S_3 NPs are shown in Figure 11 to investigate the electron

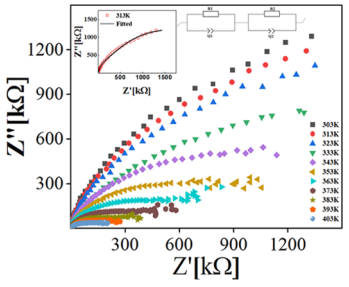

Figure 11. Nyquist plots at various temperatures (from 303 to 403 K) for the Bi_2S_3 NPs.

transport kinetic process. The plots were found to be inclined in a straight line at lower frequencies, and then a semi-circular arc was observed at higher frequencies. It denotes the charge-transfer resistance caused by charge diffusion (i.e., mass transfer), which is common in metal sulfide-based materials. The circuit diagram model also fits the Nyquist plot, as seen in the inset of Figure 11.[28]

As shown in Figure 12a,b, the change in impedance [Z' (real part) and Z'' (imaginary part)] of Bi_2S_3 NPs as a function of frequency was measured at varying temperatures. Due to the orientation and change in the dipole moment, it has been experimentally found that the dielectric constant falls with increasing frequencies and becomes constant at high frequencies. Excitation of bound electrons, vibrations of the

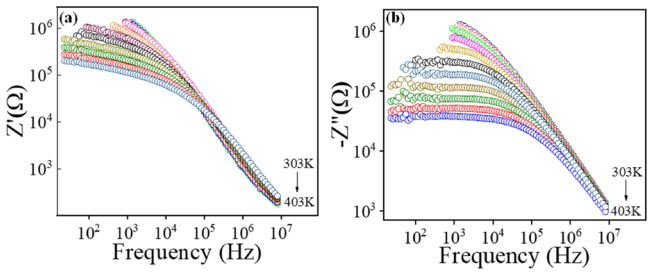

Figure 12. Plot of real part Z' (a) and imaginary part Z'' (b) of impedance at various temperatures (from 303 to 403 K).

lattice, dipole orientation, and space polarizations all contribute to the high dielectric constant at low frequencies. Because polarization does not occur quickly with the introduction of the electric field at such a high frequency owing to inertia, the dielectric constant decreases as the frequency rises.

Furthermore, owing to the increased conduction and a restricted dipole moment, the dielectric permittivity falls as the frequency rises. Z'' decreases with temperature, signifying a negative temperature coefficient of resistance and implying that conduction increases as the temperature rises. In the high-frequency range, Z' merges at all temperatures, suggesting the possibility of space charges being released. The dielectric constant refers to a dielectric substance's ability to store electrical energy. Because the polarization mechanisms quit functioning as the frequency rises, the dielectric constant falls, making it nearly impossible to follow the rapidly changing field.

At higher frequencies, the relaxation times are greater than the time it takes for the electric field to change direction, resulting in space charge polarization and conduction. As a result, the dielectric material absorbs less energy at higher frequencies. Furthermore, the AC conductivity (σ) increases as the temperature rises, implying that the electrical conductivity mechanism is a thermally triggered process and indicates the material's semiconducting nature. The $\ln(\sigma)$ versus $1000/T$ plot of Bi_2S_3 NPs is shown in Figure 13, and the variation with T follows the Arrhenius law. The activation energy of Bi_2S_3 NPs was calculated to be 0.43 eV.

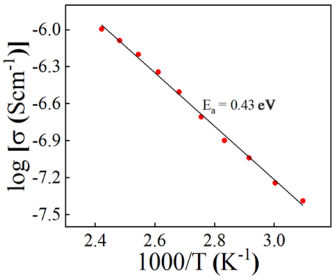

Figure 13. Temperature-dependent variation in AC conductivity.

The temperature dependence of the resistance (R/T versus $1/T$) is shown in Figure 14a using the adiabatic small-polaron hopping model. Figure 14b depicts the change of relaxation time as a function of temperature.

3.5. Dielectric Properties. Dielectric measurements were carried out on the Bi_2S_3 sample to explore the relaxation process and molecular behaviors at different frequencies and temperatures. The charge interaction between the NP surface and the microbial organism is a crucial parameter for

https://doi.org/10.1021/acsomega.2c05593
ACS Omega 2022, 7, 42438−42445

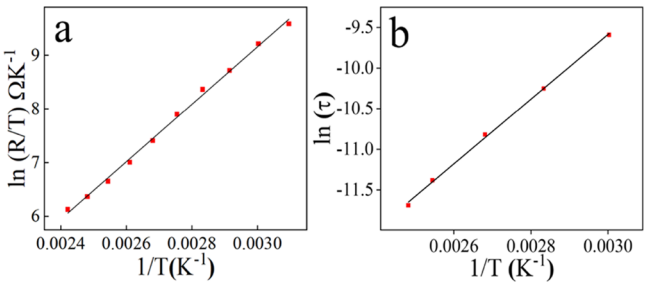

Figure 14. (a) Variation of resistance as a function of inverse temperature. Solid lines are the best fit according to the adiabatic small-polaron hopping mechanism. (b) Relaxation time of charge carriers at grain and grain boundaries plotted against the inverse of temperature.

antimicrobial properties.[29] The dielectric constant ε' (real part) was also investigated to analyze its variation with frequency at different temperatures. Figure 15 shows the

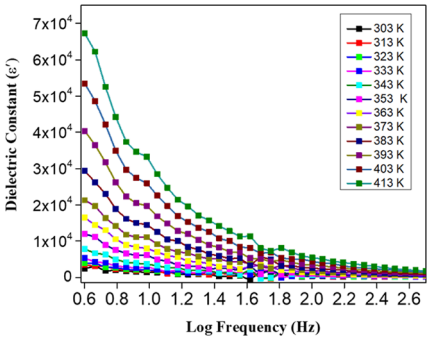

Figure 15. Plot of dielectric constant with frequency at various temperatures.

temperature-dependent characteristics of the real part of the dielectric constant. As shown, ε' tends to increase with an increasing temperature. At lower frequencies, the values of ε' are larger compared to those at higher frequencies. The plausible reason might be the following.

Dielectric polarization has many contributing factors such as interfacial and Debye orientational polarizations as well as polarizations from atoms, ions, and electrons.[30,31] At lower frequencies, the dominant contribution comes from the interfacial polarization (from grain boundaries) while the oriental polarization takes place at >10^4 Hz. The ionic, electronic, and atomic polarizations happen at higher frequencies than this. All the abovementioned polarizations contribute to the dielectric constant if the measured frequency is below the relaxation frequency.[30,31] At lower temperatures, the charge carriers at the interface boundaries contribute toward the dielectric constant. However, at higher temperatures, there is an additional inductive behavior at lower frequencies. Therefore, there is a substantial enhancement in the dielectric constant at higher temperatures.

4. CONCLUSIONS

The main aim of this study was to create water-dispersible and biocompatible Bi_2S_3 NPs that were stabilized by starch molecules. Interaction of starch with Bi_2S_3 NPs makes them stable and prevents the formation of big clusters by capping them. The crystal structure and morphology analyses, Raman vibrational mode analysis, and UV−vis spectroscopy analysis suggest the quantum confinement in NPs, and the measured values are different from the Bi_2S_3 bulk properties. The synthesized Bi_2S_3 NPs demonstrated inhibition and considerable broad-spectrum antibacterial action against human pathogenic bacterial strains (*B. subtilis*, *E. coli*, *P. aeruginosa*, and *S. aureus*). In addition, the impedance and dielectric property analyses revealed that Bi_2S_3 NPs showed significant dielectric polarizations. The starch-assisted simple synthesis method may pave a way for the growth of other metal sulfide low-dimensional nanostructures for biomedical and electronic applications.

AUTHOR INFORMATION

Corresponding Author

Jatis K. Dash − *Department of Physics, SRM University-AP, Amaravati 522502, India;* orcid.org/0000-0003-4264-3920; Email: jatis.d@srmap.edu.in, jatiskumar@gmail.com

Authors

Imran Uddin − *Department of Physics, SRM University-AP, Amaravati 522502, India*

Shaik M. Abzal − *Department of Physics, SRM University-AP, Amaravati 522502, India*

Kurapati Kalyan − *Department of Physics, SRM University-AP, Amaravati 522502, India*

Sailakshmi Janga − *Department of Physics, SRM University-AP, Amaravati 522502, India*

Ashutosh Rath − *CSIR-Institute of Minerals and Materials Technology, Bhubaneswar, Odisha 751013, India;* orcid.org/0000-0003-2559-9921

Rajkumar Patel − *Energy and Environmental Science and Engineering (EESE), Integrated Science and Engineering Division (ISED), Underwood International College, Yonsei University, Yeonsu-gu, Incheon 21983, South Korea;* orcid.org/0000-0002-3820-141X

Deepak K. Gupta − *Materials Science Group, Indira Gandhi Centre for Atomic Research, HBNI, Kalpakkam 603102, India*

T. R. Ravindran − *Materials Science Group, Indira Gandhi Centre for Atomic Research, HBNI, Kalpakkam 603102, India;* orcid.org/0000-0002-4534-8487

Hira Ateeq − *Department of Biochemistry, Aligarh Muslim University, Aligarh, Uttar Pradesh 202002, India*

Mohd Sajid Khan − *Department of Biochemistry, Aligarh Muslim University, Aligarh, Uttar Pradesh 202002, India*

Complete contact information is available at: https://pubs.acs.org/10.1021/acsomega.2c05593

Author Contributions

#I.U. and S.M.A. equally contributed to this work.

Notes

The authors declare no competing financial interest.

ACKNOWLEDGMENTS

J.K.D. and K.K. would like to acknowledge the UGC-DAE Consortium for Scientific Research, Kolkata Centre for the Collaborative Research Scheme (CRS) project (Grant No. UGC-DAE-CSR-KC/CRS/19/IBMS04/0465). I.U. acknowledges the SRM University-AP for the timely financial support to carry out this work.

https://doi.org/10.1021/acsomega.2c05593
ACS Omega 2022, 7, 42438−42445

REFERENCES

(1) Linhart, W. M.; Zelewski, S. J.; Scharoch, P.; Dybała, F.; Kudrawiec, R. Nesting-like band gap in bismuth sulfide Bi2S3. *J. Mater. Chem. C* **2021**, *9*, 13733−13738.

(2) Arumugam, J.; George, A.; Raj, A. D.; Irudayaraj, A. A.; Josephine, R. L.; Sundaram, S. J.; Al-Mohaimeed, A. M.; Al-onazi, W. A.; Elshikh, M. S.; Kaviyarasu, K. Construction and Characterization of Photodiodes prepared with Bi2S3 Nanowires. *J. Alloys Compd.* **2021**, *863*, No. 158681.

(3) Xu, J.; Li, H.; Fang, S.; Jiang, K.; Yao, H.; Fang, F.; Chen, F.; Wang, Y.; Shi, Y. Synthesis of bismuth sulfide nanobelts for high performance broadband photodetectors. *J. Mater. Chem. C* **2020**, *8*, 2102−2108.

(4) Yang, W.; Yang, J.; Zhao, K.; Gao, Q.; Liu, L.; Zhou, Z.; Hou, S.; Wang, X.; Shen, G.; Pang, X.; Xu, Q.; Wei, Z. Low-Noise Dual-Band Polarimetric Image Sensor Based on 1D Bi2 S3 Nanowire. *Adv. Sci.* **2021**, *8*, No. e2100075.

(5) Ai, K.; Liu, Y.; Liu, J.; Yuan, Q.; He, Y.; Lu, L. Large-scale synthesis of Bi_2S_3 nanodots as a contrast agent for in vivo X-ray computed tomography imaging. *Adv. Mater.* **2011**, *23*, 4886−4891.

(6) de la Parra-Arciniega, S. M.; Garcia-Gomez, N. A.; Garza-Tovar, L. L.; Garcia-Gutierrez, D. I.; Sanchez, E. M. Ultrasonic irradiation-assisted synthesis of Bi_2S_3 nanoparticles in aqueous ionic liquid at ambient condition. *Ultrason. Sonochem.* **2017**, *36*, 95−100.

(7) Motaung, M. P.; Onwudiwe, D. C.; Lei, W. Microwave-Assisted Synthesis of Bi_2S_3 and Sb2S3 Nanoparticles and Their Photoelectrochemical Properties. *ACS Omega* **2021**, *6*, 18975−18987.

(8) Zhao, W.-B.; Zhu, J.-J.; Xu, J.-Z.; Chen, H.-Y. Photochemical synthesis of Bi_2S_3 nanoflowers on an alumina template. *Inorg. Chem. Commun.* **2004**, *7*, 847−850.

(9) Abdullah, N. H.; Zainal, Z.; Silong, S.; Tahir, M. I. M.; Tan, K.-B.; Chang, S.-K. Thermal decomposition synthesis of nanorods bismuth sulphide from bismuth N-ethyl cyclohexyl dithiocarbamate complex. *Thermochim. Acta* **2016**, *632*, 37−45.

(10) Peng, B.; Cao, A.; Lv, P. In-situ stirring assisted hydrothermal synthesis of Bi2S3 nanowires on BiVO4 nanostructures for improving photocatalytic performances. *Inorg. Chem. Commun.* **2021**, *134*, No. 109012.

(11) Zhang, B.; Ye, X.; Hou, W.; Zhao, Y.; Xie, Y. Biomolecule-Assisted Synthesis and Electrochemical Hydrogen Storage of Bi2S3 Flowerlike Patterns with Well-Aligned Nanorods. *J. Phys. Chem. B* **2006**, *110*, 8978−8985.

(12) Lu, Q.; Gao, F.; Komarneni, S. Biomolecule-Assisted Synthesis of Highly Ordered Snowflakelike Structures of Bismuth Sulfide Nanorods. *J. Am. Chem. Soc.* **2004**, *126*, 54−55.

(13) Uddin, I.; Ahmad, A.; Ahmad Siddiqui, E.; Rahaman, H.; Gambhir, S. Biosynthesis of fluorescent Bi2S3 nanoparticles and their application as dual-function SPECT-CT probe for animal imaging. *Curr. Top. Med. Chem.* **2016**, *16*, 2019−2025.

(14) Uddin, I. Onsite visual detection of heavy metal contaminants using impregnated strip. *J. Photochem. Photobiol. A: Chem.* **2021**, *421*, No. 113512.

(15) Bano, S.; Raj, S. I.; Khalilullah, A.; Jaiswal, A.; Uddin, I. Selective and sensitive cation exchange reactions in the aqueous starch capped ZnS nanoparticles with tunable composition, band gap and color for the detection and estimation of Pb^{2+}, Cu^{2+} and Hg^{2+}. *J. Photochem. Photobiol. A Chem.* **2021**, *405*, No. 112925.

(16) Raj, S. I.; Jaiswal, A.; Uddin, I. Ultrasmall aqueous starch-capped CuS quantum dots with tunable localized surface plasmon resonance and composition for the selective and sensitive detection of mercury (II) ions. *RSC Adv.* **2020**, *10*, 14050−14059.

(17) Li, J.; Li, Z.; Liu, X.; Li, C.; Zheng, Y.; Yeung, K. W. K.; Cui, Z.; Liang, Y.; Zhu, S.; Hu, W. J. N. Interfacial engineering of Bi_2S_3 /$Ti_3C_2T_x$ MXene based on work function for rapid photo-excited bacteria-killing. *Nat. Commun.* **2021**, *12*, 1224.

(18) Peter, L. M.; Wijayantha, K. U.; Riley, D. J.; Waggett, J. P. Band-edge tuning in self-assembled layers of Bi2S3 nanoparticles used to photosensitize nanocrystalline TiO_2. *J. Phys. Chem. B* **2003**, *107*, 8378−8381.

(19) Zhao, W.-B.; Zhu, J.-J.; Zhao, Y.; Chen, H.-Y. Photochemical synthesis and characterization of Bi_2S_3 nanofibers. *Mater. Sci. Eng., B* **2004**, *110*, 307−313.

(20) Cheng, H.; Huang, B.; Qin, X.; Zhang, X.; Dai, Y. A controlled anion exchange strategy to synthesize Bi_2S_3 nanocrystals/BiOCl hybrid architectures with efficient visible light photoactivity. *Chem. Commun.* **2012**, *48*, 97−99.

(21) The XRD patterns were indexed with reference to the crystal structures from the PCPDFWIN: Bi_2S_3 (# 17−0320). *PCPDFWIN: Bi_2S_3 (# 17−0320)*.

(22) Benher, Z. R.; Gardonio, S.; Fanetti, M.; Moras, P.; Kundu, A. K.; Bigi, C.; Valant, M. Electronic properties of phases in the quasi-binary Bi_2Se_3 − Bi_2S_3 system. *J. Mater. Chem. C* **2021**, *9*, 3058−3064.

(23) Zumeta-Dubé, I.; Ortiz-Quiñonez, J.-L.; Díaz, D.; Trallero-Giner, C.; Ruiz-Ruiz, V.-F. First Order Raman Scattering in Bulk Bi_2S_3 and Quantum Dots: Reconsidering Controversial Interpretations. *J. Phys. Chem. C* **2014**, *118*, 30244−30252.

(24) Pfannemüller, B.; Mayerhöfer, H.; Schulz, R. C. Conformation of amylose in aqueous solution: optical rotatory dispersion and circular dichroism of amylose−iodine complexes and dependence on chain length of retrogradation of amylose. *Biopolymers* **1971**, *10*, 243−261.

(25) Pfannemüller, B. Ordered arrangements in solutions of amylose-iodine complexes derived from free and terminally fixed amylose chains. *Carbohydr. Res.* **1978**, *61*, 41−52.

(26) Uddin, I. Mechanistic approach to study conjugation of nanoparticles for biomedical applications. *Spectrochim. Acta, Part A: Mol. Biomol. Spectrosc.* **2018**, *202*, 238−243.

(27) Blair, J. M. A.; Webber, M. A.; Baylay, A. J.; Ogbolu, D. O.; Piddock, L. J. V. Molecular mechanisms of antibiotic resistance. *Nat. Rev. Microbiol.* **2015**, *13*, 42−51.

(28) Ahmad, M.; Rafiq, M. A.; Rasool, K.; Imran, Z.; Hasan, M. M. Dielectric and transport properties of bismuth sulfide prepared by solid state reaction method. *J. Appl. Phys.* **2013**, *113*, No. 043704.

(29) Rajendiran, K.; Zhao, Z.; Pei, D. S.; Fu, A. Antimicrobial Activity and Mechanism of Functionalized Quantum Dots. *Polymers (Basel)* **2019**, *11*, 1670.

(30) Rahman, A. U.; Rafiq, M. A.; Karim, S.; Maaz, K.; Siddique, M.; Hasan, M. M. Reduced conductivity and enhancement of Debye orientational polarization in lanthanum doped cobalt ferrite nanoparticles. *Phys. B* **2011**, *406*, 4393−4399.

(31) Akhtar, M. J.; Younas, M. Structural and transport properties of nanocrystalline $MnFe_2O_4$ synthesized by co-precipitation method. *Solid State Sci.* **2012**, *14*, 1536−1542.

https://doi.org/10.1021/acsomega.2c05593
ACS Omega 2022, 7, 42438−42445